Journal of Materials Chemistry C

PAPER

View Article Online
View Journal | View Issue

Cite this: J. Mater. Chem. C, 2016, 4, 559

Synthesis, electronic transport and optical properties of Si:α-Fe_2O_3 single crystals†

Alexander J. E. Rettie,[a] William D. Chemelewski,[b] Bryan R. Wygant,[c] Jeffrey Lindemuth,[d] Jung-Fu Lin,[ef] David Eisenberg,[g] Carolyn S. Brauer,[h] Timothy J. Johnson,[h] Toya N. Beiswenger,[h] Richard D. Ash,[i] Xiang Li,[b] Jianshi Zhou[b] and C. Buddie Mullins*[abc]

Received 16th October 2015,
Accepted 11th December 2015

DOI: 10.1039/c5tc03368c

www.rsc.org/MaterialsC

We report the synthesis of silicon-doped hematite (Si:α-Fe_2O_3) single crystals *via* chemical vapor transport, with Si incorporation on the order of 10^{19} cm^{-3}. The conductivity, Seebeck and Hall effect were measured in the basal plane between 200 and 400 K. Distinct differences in electron transport were observed above and below the magnetic transition temperature of hematite at ~265 K (the Morin transition, T_M). Above 265 K, transport was found to agree with the adiabatic small-polaron model, the conductivity was characterized by an activation energy of ~100 meV and the Hall effect was dominated by the weak ferromagnetism of the material. A room temperature electron drift mobility of ~10^{-2} cm^2 V^{-1} s^{-1} was estimated. Below T_M, the activation energy increased to ~160 meV and a conventional Hall coefficient could be determined. In this regime, the Hall coefficient was negative and the corresponding Hall mobility was temperature-independent with a value of ~10^{-1} cm^2 V^{-1} s^{-1}. Seebeck coefficient measurements indicated that the silicon donors were fully ionized in the temperature range studied. Finally, we observed a broad infrared absorption upon doping and tentatively assign the feature at ~0.8 eV to photon-assisted small-polaron hops. These results are discussed in the context of existing hematite transport studies.

1. Introduction

Photoelectrochemical (PEC) cells offer a potential route to clean, renewable hydrogen by splitting water using solar energy.[1] Metal oxide semiconductors are a promising class of materials for photoelectrodes due to their stability and relative abundance. Hematite (α-Fe_2O_3) is one of the most studied, owing to its attractive band gap of ~2.1 eV and stability in basic electrolytes.[2] However, its notoriously poor transport properties are a bottleneck to higher efficiencies, specifically severe recombination on the order of picoseconds[3] and low carrier mobilities (<1 cm^2 V^{-1} s^{-1}).[4]

Hence, doping and nanostructuring[5–9] have been vital in optimizing this material's PEC performance. n-type doping of α-Fe_2O_3 has been achieved by substitution of Fe^{3+} with various M^{4+} ions, *e.g.* Si, Sn, Ti, Zr or Ge. Ubiquitous in nature, bulk charge transport in hematite also plays an important role in many geochemical processes.[10,11] Electronic transport agrees well with the small-polaron model[12,13] but a thorough analysis in this framework around room temperature – where PEC cells would operate – has not been performed. Recent work by our group utilized conductivity, Seebeck and Hall effect measurements as functions of temperature to probe the nature of small polarons in single crystals of another promising photoelectrode: tungsten-doped bismuth vanadate (W:$BiVO_4$).[14,15]

Si^{4+} has been shown to be an effective n-type dopant in hematite photoanodes for water oxidation.[16–18] Despite this, the electronic properties of silicon-doped single crystal hematite have not been reported. Recently, Zhao *et al.*[12] synthesized heavily Ti^{4+}-doped (3–9 at%) epitaxial thin films *via* oxygen-assisted molecular beam epitaxy. Good agreement with the small-polaron model was observed from 140 to 300 K. The Hall effect was analyzed using the conventional semiconductor framework, yielding a Hall mobility of ~10^{-1} cm^2 V^{-1} s^{-1} that was temperature independent from 190 to 290 K. Additionally, Gharibi *et al.* measured the conductivity and Seebeck coefficient of single crystals of Ti:α-Fe_2O_3 at elevated temperatures and

[a] McKetta Department of Chemical Engineering, The University of Texas at Austin, TX 78712, USA. E-mail: mullins@che.utexas.edu
[b] Texas Materials Institute, The University of Texas at Austin, TX 78712, USA
[c] Department of Chemistry, The University of Texas at Austin, TX 78712, USA
[d] Lake Shore Cryotronics, Westerville, OH 43082, USA
[e] Department of Geological Sciences, The University of Texas at Austin, TX 78712, USA
[f] Center for High Pressure Science and Technology Advanced Research (HPSTAR), Shanghai 201900, China
[g] Van't Hoff Institute for Molecular Sciences, University of Amsterdam, Amsterdam, 1098 XH, The Netherlands
[h] Pacific Northwest National Laboratory, Richland, WA 99352, USA
[i] Department of Geology, University of Maryland, College Park, MD 20742, USA

† Electronic supplementary information (ESI) available: Laue XRD spot patterns, Raman spectra analysis, additional transport data and calculations. See DOI: 10.1039/c5tc03368c

concluded that small-polaron hopping was in the non-adiabatic regime at 780 K.[13] However, this assignment is questionable, as the non-adiabatic regime requires a transfer integral that is too small for most real materials.[19] In both of these prior reports the conductivity and either the Seebeck or Hall effect were measured as functions of temperature. The measurement of all three techniques on the same samples is most desirable for complete characterization of small-polaron hopping processes.[14]

In addition to the identifying characteristics of their electronic transport, small polarons possess unique optical properties. Specifically, photon-assisted hopping may occur, which manifests as broad infrared absorption.[19] Absorption bands corresponding to this process have been observed in reduced rutile TiO_2,[20] rare-earth manganites,[21] titanates[22] and reduced $LiNbO_3$.[23]

Here, we describe the synthesis and characterization of Si:α-Fe_2O_3 single crystals by chemical vapor transport. Crystal quality and composition was evaluated by X-ray diffraction (XRD), Raman spectroscopy and laser ablation inductively-coupled plasma mass spectrometry (LA-ICP-MS). The conductivity, Seebeck coefficient and Hall effect were measured in the basal plane from 200 to 400 K. These data were analyzed within the adiabatic small-polaron hopping model and are discussed in the context of other doped hematite transport studies. Finally, the reflectance of Si:α-Fe_2O_3 at low energies was probed to provide further evidence for the creation of small polarons. To the best of our knowledge, this is the first report concerning the electronic properties of Si:α-Fe_2O_3 single crystals and mid-IR absorption of doped hematite. In this article, the basal, (0001)- and *c*-plane will be used interchangeably in this article to avoid repetition.

2. Experimental methods

2.1 Synthesis

Chemical vapor transport (CVT) was used to grow millimeter-sized Si:α-Fe_2O_3 crystals for transport measurements.[13,24] α-Fe_2O_3 (99.995%, Sigma-Aldrich) was transported at 1040 and 930 °C in the hot and cold zones respectively using tellurium tetrachloride ($TeCl_4$, 99.9%, Alfa Aesar) as the transport agent in a 3-zone tube furnace (ThermCraft). Silica tubes were charged with approximately 1 g of hematite and 5 mg cm^{-3} of $TeCl_4$. As $TeCl_4$ is air and moisture sensitive, this compound was loaded into the tubes in an Ar-filled glovebox, before being evacuated to *ca.* 10^{-5} Torr and sealed. Back-transport (inverted temperature gradient) was performed for 24 h before the growth, which lasted 10–13 days. As will be discussed in Section 3.2, the resulting "undoped" crystals were moderately conductive, an unexpected result as we had not intentionally added any impurities. Silicon dopants were detected during compositional testing of the grown crystals, presumably provided by the walls of the silica tubes. Additionally, in an effort to synthesize Ti-doped hematite single crystals, we added enough Ti metal (99.7%, Pfaltz and Bauer) to replace 1% of the Fe sites (60 mg) in some cases.

The silica tubes were cleaned to remove small dust particles and imperfections that could act as nucleation sites using the following procedure: an HF acid rinse followed by soaking in aqua regia for 3 h, before another HF acid rinse and finally drying under vacuum overnight. De-ionized water was used throughout. Post-reaction, the tube was opened in a fume hood and the resultant crystals washed and sonicated in DI water and acetone. Finally, all crystals were annealed in air at 500 °C for 1 h to convert any undesired iron oxide phases to hematite.

2.2 Compositional characterization

Powder X-ray diffraction (XRD) was performed using a Philips X'Pert diffractometer equipped with monochromatic Cu Kα X-rays (λ = 1.54056 Å). Laue back-reflection XRD was utilized to determine crystal quality and orientation using a Rigaku Geigerflex with Mo radiation. Samples were oriented within 2 degrees of the principal axes. An optical Raman system with a Verdi V2 532 nm green laser, Andor spectrometer, iCCD detector and an 1800 grating was used for the Raman scattering measurements. Crystal composition was determined using a New Wave Research UP213 (213 nm) laser-ablation system coupled to a Thermo-Finnigan Element2 inductively coupled plasma mass spectrometer (LA-ICP-MS) at the University of Maryland. Typical laser fluences and repetition rates used were ~3 J cm^{-2} and 7 Hz respectively. Samples were mounted on double sided tape. Material was ablated into a stream of helium (*ca.* 0.6 L min^{-1}), which was then mixed with Ar (*ca.* 0.9 L min^{-1}) before introduction into the mass spectrometer. Laser ablation was either using spot analyses, for high precision determination in a limited area, or by rastering to test for the degree of heterogeneity over the sample.

Samples were compared with the NIST610 alumino-silicate glass standard, USGS BHVO2g and BCR2g basaltic standards when measuring the entire range of trace elements. Standards were analysed in identical fashion to their respective samples. For the determination of Si abundance these standards were compared to the low-alloy V–Cr steel NIST 1263a to ensure the validity of the silicate glasses for the measurement of non-silicate matrix (*i.e.* hematite). The results for NIST1263a were 2–10% higher than the certified value, but this material has proven to be problematic for *in situ* analysis due to heterogeneity, but may provide some guidance as to the worst case scenario for accuracy when comparing silicates to metals. We expect the laser coupling of the oxide and silicate to be more similar than that of the silicate and steel.

All samples were cleaned with an ablation pass or brief pulse of the laser prior to the data gathering ablation. Gas background measurements were taken for 20 seconds prior to sample analysis. Iron (^{57}Fe) was used as an internal standard in all cases and data was reduced using LAMTRACE software. Upper limits for concentration were calculated by setting the detection limit for any given isotope measured as 3 times the mean measured gas background.

For trace element measurement at low resolution ($M/\Delta M$ = 300) sample spot-sizes ranged from 30 to 55 μm, depending upon the size of the sample and the elements being determined. A larger spot-size, 100 μm, was used for the determination of Si abundances at medium resolution ($M/\Delta M$ = 3000). Medium resolution enabled

the Si mass peaks (28, 29 and 30 amu) to be resolved from the isobaric interferences from $^{56}Fe^{++}$, N_2^+ and CO^+ signals.

2.3 Magnetic and transport measurements

4-point conductivity and AC field Hall effect measurements were conducted at Lake Shore Cryotronics on an 8404 AC/DC Hall measurement system and DC field Hall effect experiments up to 9 T on a 9709A model system. Magnetic fields were applied perpendicular to the basal plane. Some room temperature conductivity measurements were performed on a Keithley 4200-SCS. Ohmic contact was achieved using In–Ga eutectic (Sigma-Aldrich) or e-beam evaporated Ag metal pads, attached to fine Cu wires with Ag epoxy (EPO-TEK). Example *i*–*V* curves are given in the ESI† (Fig. S1). Use of just Ag epoxy produced highly resistive, non-ohmic contacts. Evaporated contacts were defined on the small crystals using hand-made wire masks. Contact geometry was either 4-point van der Pauw on plate-like samples or 4-point collinear on bar shaped samples. Measurement of the Seebeck coefficient was performed using a laboratory-built apparatus at UT Austin. In the case of the Seebeck measurements, high quality contacts were made by evaporating Ag or painting InGa over opposite crystal faces. All transport measurements were conducted in the basal plane. Magnetic properties were obtained using a Physical Property Measurement System (PPMS, Quantum Design) with a vibrating sample magnetometer (VSM) attachment.

2.4 Optical properties

Crystals were ground to micron-size powders for optical characterization and either used directly, or mixed with KBr and pressed into pellets. Diffuse reflectance UV-vis-NIR spectra were measured with a Cary 500 spectrophotometer attached to an integrating sphere (Labsphere DRA-CA-5500). A Tensor 37 FT-IR spectrometer (Bruker Optics) equipped with an A562 integrating sphere at Pacific Northwest National Laboratory was used to measure quantitative reflectance from 1.3 to 16.6 μm.[25,26] All optical measurements were performed at room temperature. Later in this article we compare the optical properties of our Si-doped hematite to those of Ti-doped hematite (Section 3.4). The polycrystalline Ti:α-Fe_2O_3 powder was synthesized by conventional solid-state methods after Morin.[27] α-Fe_2O_3 (99.995%, Sigma-Aldrich) and TiO_2 (99.9+%, US Research Nanomaterials, Inc.) powders were ground and annealed at 1100 °C in air for 16 h. Enough TiO_2 was added to replace 2% of Fe sites with Ti in α-Fe_2O_3.

2.5 Methodology

Inherent to CVT and flux growth techniques, local variations in temperature and reactant flux in the reaction vessel may result in variation in composition from crystal to crystal. Thus, it was vital to grow millimeter-sized samples, on which a battery of characterization and transport measurements could be made for comparison and analysis. Generally, once large crystals were identified, their quality was checked by XRD and Raman spectroscopy. Seebeck coefficient measurements were then performed on the crystals, before being diced and polished into smaller samples for conductivity and Hall effect measurements. Finally these samples were analyzed using LA-ICP-MS to determine their composition and doping homogeneity.

3. Results and discussion

3.1 Synthesis

The CVT process produced black, specular crystals ranging from thin (~40 μm) platelets with large (up to 10 mm^2) (0001) faces to prismatic samples hundreds of microns in thickness (Fig. 1). Once a large (0001)-plane was identified by Laue back-reflection XRD, crystals were cut and polished along principal axes relative to it. Laue XRD was employed to check orientation and quality on several areas of the crystals (see Fig. S2 in the ESI† for an example Laue pattern). Crystals grew in both ends of the tube, as is commonly observed in the CVT growth of α-Fe_2O_3.[28,29] The material turned a characteristic dark red color upon grinding with a mortar and pestle.

3.2 Phase and composition

X-ray diffraction (XRD) spectra for pulverized crystals could only be indexed to α-Fe_2O_3 (PDF # 01-071-5088) as shown in Fig. 2. The crystal structure can be described as rhombohedral (illustrated in Fig. 3a) or distorted hexagonal ($R\bar{3}c$ space group, a = 5.035 Å, c = 13.75 Å),[30] consisting of edge-sharing FeO_6 octahedra in the basal planes and face-sharing perpendicular to them.[31] One third of the Fe sites are vacant, forming the hexagonal arrangement Fe atoms illustrated in Fig. 3b. As we will deal with transport in the basal planes, we will refer exclusively to the hexagonal structure in this article.

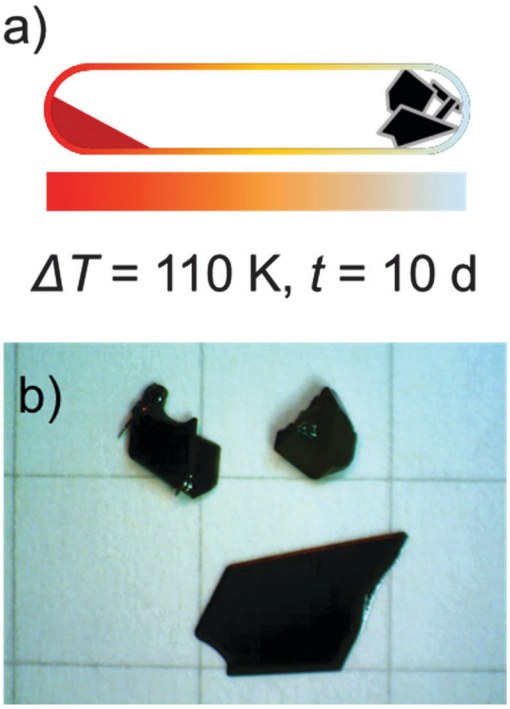

Fig. 1 (a) Cartoon of CVT synthesis showing temperature gradient, ΔT and transport duration, t. (b) Photograph of typical Si:α-Fe_2O_3 crystals grown by CVT on 5 × 5 mm^2 square paper.

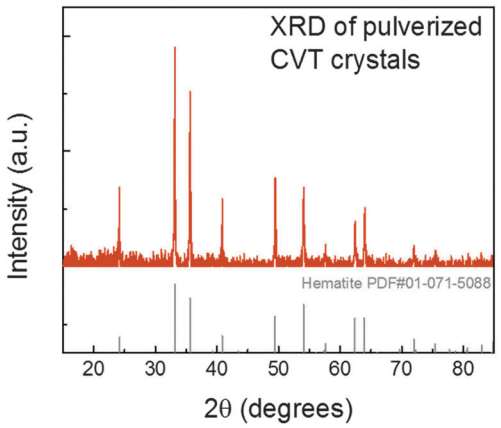

Fig. 2 Powder XRD of pulverized Si:α-Fe_2O_3 crystals.

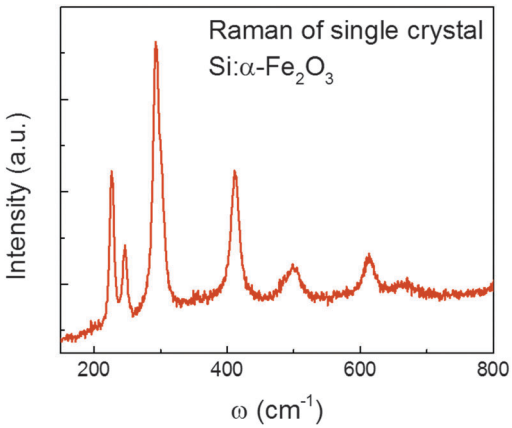

Fig. 4 Raman spectrum of single crystalline Si:α-Fe_2O_3.

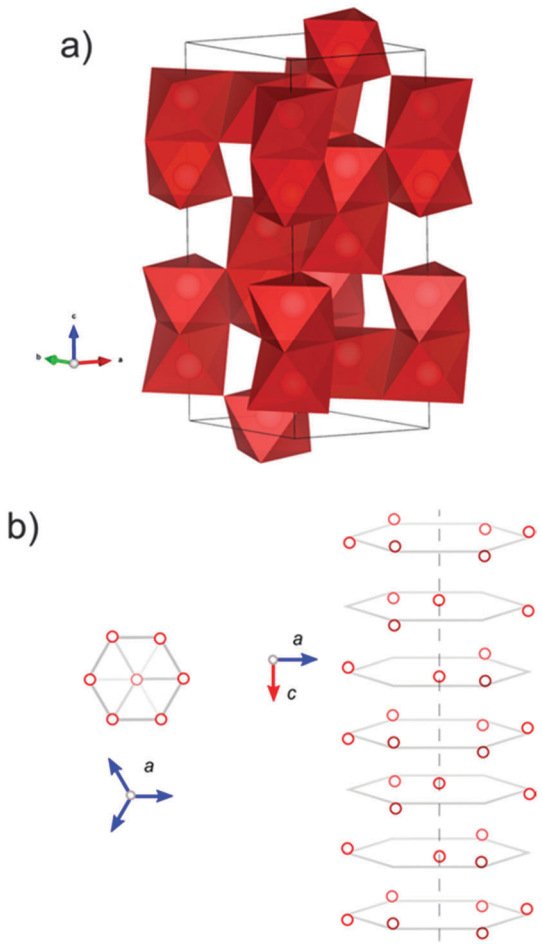

Fig. 3 (a) Rhombohedral unit cell of hematite showing FeO_6 units. Created using VESTA software.[38] (b) Cartoon of the hexagonal arrangement of Fe atoms, depicting basal planes.

Raman spectroscopy showed the expected vibrational modes for hematite: two A_{1g} modes at ~226 and 500 and five E_g modes at 245, 283, 293, 300 and 612 cm^{-1} respectively (Fig. 4).[31–33] The 293 and 300 cm^{-1} bands can only be resolved at low temperature.[34] The weak feature at ~660 cm^{-1} has been assigned to an IR-active and Raman-inactive E_u(LO) mode in synthetic single crystals[35] and high purity (99.998%) α-Fe_2O_3 powder.[33] Moderate laser powers can convert other iron oxide phases to hematite, complicating their detection.[34] Therefore, low powers (10 mW) and long acquisition times (~6 min) were employed. In one large crystal, a weak feature at ~670 cm^{-1} was observed, possibly corresponding to either magnetite or maghemite. Annealing in air at 500 °C or intense laser excitation is known to convert these phases to hematite, which we confirmed in this sample (Fig. S3 in the ESI†). This thermal treatment did not noticeably affect the crystallinity or electronic properties of the crystals and so was performed on all as-grown samples to ensure phase purity.

The initial materials we intended to synthesize were insulating, undoped α-Fe_2O_3 single crystals and relatively conductive Ti-doped α-Fe_2O_3, grown with the addition of Ti metal. Surprisingly, the resulting crystals in the "undoped' case, were moderately conductive (2-point resistance measurements were in the kΩ range) and n-type by Seebeck effect measurements. The level of impurity incorporation in the grown crystals was too low (<1 at%) to induce changes detectable by XRD or Raman spectroscopy; so LA-ICP-MS was used to determine the major n-type impurity in the crystals. Silicon was found to be the dominant donor impurity in all samples on the order of ~10^{19} cm^{-3} or ~0.05% based on Fe substitution (see Section S2 in the ESI† for details of compositional testing), presumably supplied by the walls of the silica tubes used for growth. This is plausible, as SiO_2 can be transported at temperatures greater than 900 °C using various halogens,[24] but is at odds with several reports in the literature using identical or similar synthesis conditions, who reported insulating (resistivity >10^5 Ω cm) undoped α-Fe_2O_3.[13,36,37] As silica is ever-present in these syntheses, we do not understand this discrepancy at present. Interestingly, when Ti metal was added to the reaction vessel, only trace quantities (<20 ppm) were present in the crystals, indicating very inefficient Ti-incorporation by this method.

3.3 Magnetic properties

The magnetic structure of hematite has long been of interest,[39] and is known to be linked to its electronic transport.[2,40] Between ~265 and ~960 K, α-Fe_2O_3 is a weak ferromagnet

with spins slightly canted in the basal plane. Below 265 K, termed the Morin transition (T_M), spins re-order to lie parallel to the *c*-axis in an antiferromagnetic arrangement, due to the competition between magnetic-dipole and single-ion anisotropy energies.[41] We will refer to these regimes as the weak ferromagnetic state (WFS) and the antiferromagnetic state (AFS) respectively. Above 955 K (the Néel temperature), hematite is paramagnetic.[42]

The magnetization *vs.* temperature of a Si:α-Fe_2O_3 single crystal is shown in Fig. 5, and was in accord with the magnetic properties reported for pure α-Fe_2O_3.[42] Although some M^{4+} dopants can significantly depress T_M, incorporation of up to 1% Si has been shown to have only minor effects on this magnetic transition temperature.[43] The magnitude of the magnetic moment, *M* was in good agreement with the study of Flanders and Remeika,[44] who showed that *M* was relatively unchanged over a wide range of dopants and doping levels in flux-grown α-Fe_2O_3 single crystals.

3.4 Electronic transport

3.4.1 Conductivity. The DC conductivity from 200 to 400 K showed semiconducting behavior, increasing by ~1.5 orders of magnitude over this temperature range (Fig. 6). These data were fit to the adiabatic small-polaron conductivity equation:[45]

$$\sigma = \sigma_0 \exp(-E_\sigma/k_B T), \quad (1)$$

where, σ is the temperature-dependent conductivity, σ_0 is a temperature-dependent pre-factor, E_σ is the conductivity activation energy, k_B is the Boltzmann constant, and T is the absolute temperature.

Plotting σT *vs.* reciprocal temperature should yield linear fits representing hopping regimes with constant activation energy in accord with eqn (1). Analysis revealed two linear regimes that were discontinuous at the characteristic Morin or "spin-flop" transition at 265 K as seen in Fig. 7. No noticeable hysteresis in the conductivity was observed upon either cooling or heating through T_M. The relevant fitting parameters in eqn (1) are summarized in Table 1. First, we will discuss the high temperature regime.

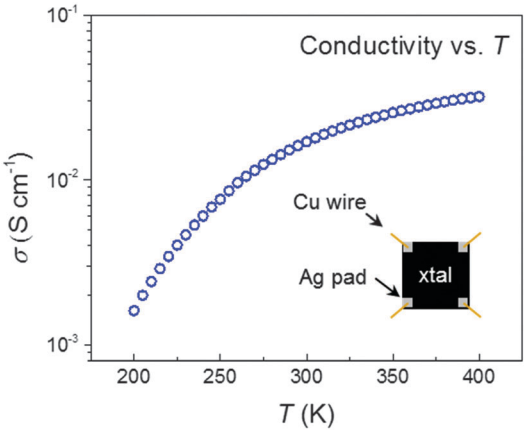

Fig. 6 Conductivity *versus* temperature for a Si:α-Fe_2O_3 ([Si] = 2×10^{19} cm^{-3}) crystal in the basal plane.

The measured activation energy of ~100 meV in the WFS was in excellent agreement with previous experimental values for n-type α-Fe_2O_3.[12,13] It was also consistent with *ab initio* calculations for adiabatic transfers between nearest neighbor Fe ions in the basal plane.[46] The excess electron donated by Si^{4+} is predicted to localize on a nearby Fe^{3+} ion,[47] reducing it to Fe^{2+}. Hopping then occurs between Fe^{2+} and Fe^{3+} sites. Estimation of the adiabatic pre-factor yielded $\sigma_0 T = 440$ S cm^{-1} K. Multiplication of σ_0 by the absolute temperature yields a temperature-independent term, useful for comparison between different temperature regimes (calculation details in the ESI†). Comparison with the measured pre-factor in Table 1 again supported the use of the adiabatic model. Note that the low donor concentration in our crystals means that σ_0 is significantly smaller than that for intrinsic small-polaron hopping.[48,49]

Below T_M, both E_σ and $\sigma_0 T$ increased significantly (Table 1 and Fig. 7). Interestingly, this behavior does not appear to have been previously reported – likely due to the WFS persisting

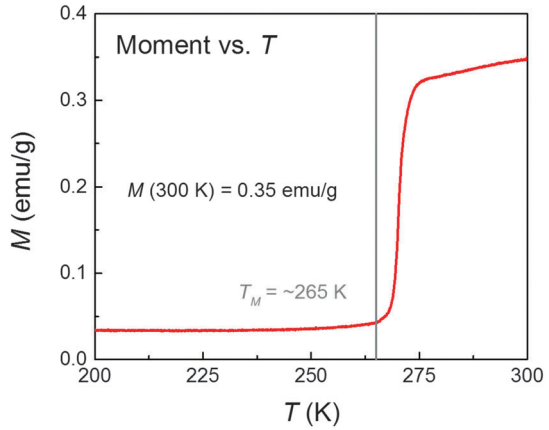

Fig. 5 Magnetization *vs.* temperature for a Si:α-Fe_2O_3 single crystal ([Si] = ~2×10^{19} cm^{-3}). The magnetic field was 1000 Oe and applied in the basal plane (easy axis), *i.e.* perpendicular to the *c*-axis.

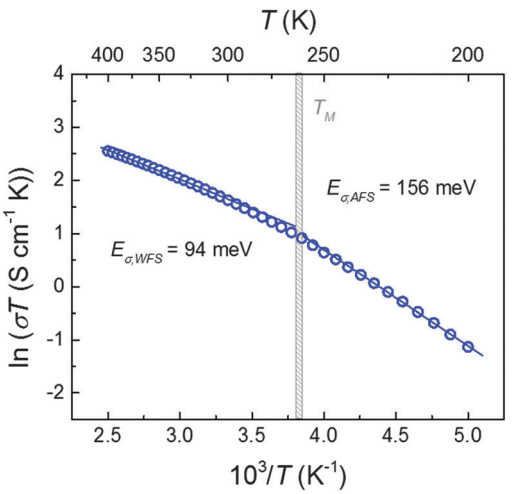

Fig. 7 Fitting of the conductivity to eqn (1) in the main text. The Morin transition temperature, T_M is indicated at ~265 K.

Table 1 Adiabatic small-polaron fitting parameters of data in Fig. 7. WFS: weak ferromagnetic state. AFS: antiferromagnetic state

	E_σ (meV)	$\sigma_0 T$ (S cm^{-1} K)
WFS ($T > 265$ K)	94 ± 1	199 ± 1
AFS ($T < 265$ K)	156 ± 1	2721 ± 26

down to very low temperatures in heavily doped samples,[43] which are often utilized in transport studies around room temperature.[12,27] We interpret this observation within the small-polaron model as an increase in the hopping barrier brought about by the flopping of spins from slightly canted in the basal plane to parallel to the *c*-axis (Fig. 5).

The magnetic nature of a carrier's initial and final sites has an effect on the hopping rate and the increased activation energy may suggest that hopping between Fe ions with antiparallel spins occurs in the AFS[50] (*i.e.* inter-plane hopping between sites with antiparallel spins), while in-plane hops between near-parallel spin Fe sites dominate transport in the WFS. However, this hypothesis raises the question: why are these more difficult hops preferred in the AFS over the in-plane transfers which are still presumably available? Theoretical calculations are needed to provide guidance on this issue.

3.4.2 Seebeck coefficient. The Seebeck coefficient, S, in the basal plane was large and negative, consistent with the crystal being an n-type semiconductor (Fig. 8). The lack of a significant change around the spin-flop transition ($\sim$265 K) is consistent with the magnetic contributions to the Seebeck coefficient being small at relatively low temperatures for small-polaron conductors.[19,51] The magnitude of the Seebeck coefficient increased with increasing temperature in this temperature range, as was also observed in the basal plane of Ti:α-Fe_2O_3 single crystals.[13]

This behavior indicates that the carrier concentration is constant and the main temperature-dependent contribution to S is the re-distribution of carriers among available transport states. Alternatively stated, the Si dopants are fully ionized, and there is no activation energy associated with carrier generation. This allows estimation[45] of the drift mobility using eqn (2),

$$\mu_d = [ega^2\nu_0/(k_B T)]\exp(-(E_\sigma)/(k_B T)) \quad (2)$$

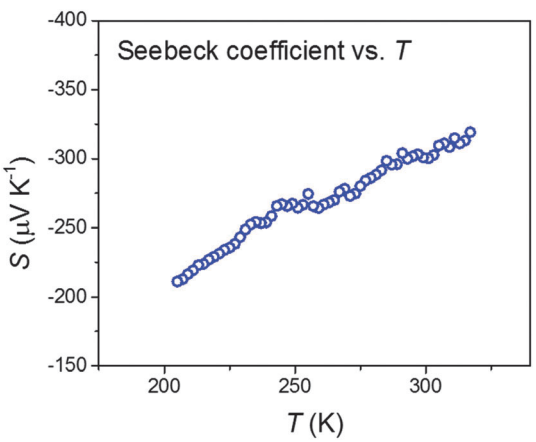

Fig. 8 Seebeck coefficient measured in the basal plane *vs.* temperature.

where, μ_d is the drift mobility, e is the electronic charge, g is a geometric pre-factor, a is the hopping distance and ν_0 is the characteristic phonon frequency. A value of 10^{-2} cm^2 V^{-1} s^{-1} was calculated at 300 K, which is in good agreement with that calculated assuming the donor concentration is equal to the Si concentration (Section S2 in the ESI†).

3.4.3 Hall effect. Considerable variation exists in the literature regarding the Hall effect in hematite. In some cases, anomalous behavior commonly seen in ferromagnets due to magnetization has been observed with the field applied in the *c*-axis.[52] However in most cases, no Hall effect was observed with this field orientation.[53–55] Additionally, in heavily doped (>1%) epitaxial films, conventional Hall effect behavior (*i.e.* the Hall voltage being linear with applied field) was found from 190 to 290 K.[12]

We observed an anomalous Hall effect above the Morin transition with the applied field parallel to the *c*-axis, presumably due to the weak magnetization of the material. The Hall resistivity is given by:[52,56]

$$\rho_{Hall} = V_{Hall}t/i = R_{Hall}B \quad (3)$$

where, ρ_{Hall} is the Hall resistivity, V_{Hall} is the transverse Hall voltage, t is the sample thickness, i is the applied current, R_{Hall} is the Hall coefficient and B is the applied field. The field-dependent signal above T_M is shown in Fig. 9a and resembles the magnetic behavior of the single crystals (Fig. S4 in the ESI†). Thus, we conclude that that the Hall voltages are primarily due to the magnetization of the material in this regime.

Below T_M, the Hall resistivity was linear with field at low fields, but large anomalous behavior returned once a critical field was applied (indicated by arrows in Fig. 9b). This behavior correlates well with the field-induced spin-flop transition from the AFS to WFS that occurs in hematite when a sufficient field is applied parallel to *c*-axis.[42,57,58] For ease of data collection, the AC field Hall effect (RMS field of 0.67 T) was used to discern the Hall voltages at $T < T_M$.

The Hall coefficient over the temperature range 200–255 K measured by the AC field Hall effect technique are shown in Fig. 10. R_{Hall} was negative in this temperature range, consistent with the sign of the Seebeck coefficient. An anomalously-signed Hall coefficient can occur for small-polaron conduction, where the sign depends on the product of transfer energies and number of members in the hopping loop.[19] However, for electron hopping in a mostly empty band, the Hall coefficient's sign should be negative for all n.

Finally, the Hall effect mobility, μ_{Hall} was calculated using

$$\mu_{Hall} = R_{Hall}\sigma, \quad (4)$$

and was largely independent of temperature with a value of $\sim 10^{-1}$ cm^2 V^{-1} s^{-1}. These observations are consistent with small-polaronic transport, though we note that we cannot directly compare the drift and Hall mobilities due to the effects of the spin-flop transition.

The conventional Hall effect in the WFS observed by Zhao *et al.* in their epitaxial thin films may indicate that there are additional effects of high Ti concentrations that affect the magneto-transport properties of hematite. That this behavior

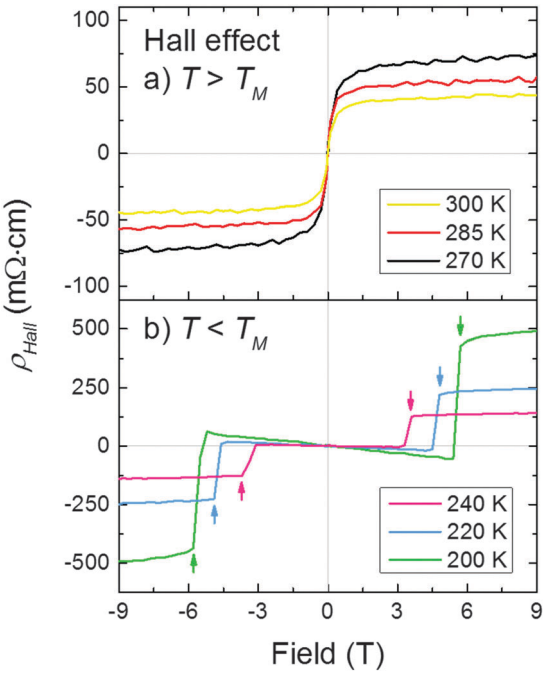

Fig. 9 Hall resistivity *vs.* applied field at various temperatures (a) above and (b) below the Morin transition.

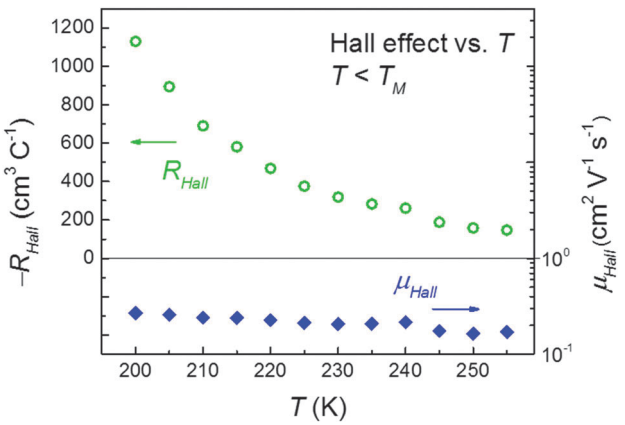

Fig. 10 Hall coefficient and mobility *versus* temperature in the AFS of hematite.

is not observed in bulk single crystal or polycrystalline α-Fe_2O_3 is not surprising, since high Ti concentrations are not usually attainable using bulk single crystal growth techniques (typically <1 at%). Further investigations of transport as a function of doping over a wide range would therefore be extremely interesting. Though nominally achievable in ceramics, the effects of M^{4+}-incorporation are often dampened in polycrystalline samples, *e.g.* the suppression of the Morin transition temperature.[43] This is likely because only a small fraction of the dopants are replacing Fe^{3+} in the lattice.

3.5 Optical characterization

To investigate changes in the optical spectrum of hematite upon incorporation of Si, we performed measurements on pristine α-Fe_2O_3 powder (99.995%, Sigma-Aldrich), ground Si:α-Fe_2O_3 crystals grown by CVT and Ti:α-Fe_2O_3 powder synthesized by a solid-state route after Morin[27] (Fig. 11). Three main features were observed in the visible-near infrared region (Fig. 11a). The band gap, E_g (~2.15 eV) and features at ~1.75 and ~1.4 eV were indicative of hematite. The latter features have been assigned to (1) $^6A_1 \rightarrow {}^4E$ and (2) $^6A_1 \rightarrow {}^4A_2$ crystal field or ligand transitions, respectively.[59] A fourth, broad feature could be observed at energies <1.0 eV. This was first reported by Morin[60] in 1% Ti-doped polycrystalline thin films and attributed to transitions between Fe and Ti donor levels. That this feature was also observed in our Si:α-Fe_2O_3 crystals implies similar energetics for Si dopants.

Of special interest was low energy absorption in the mid-IR (Fig. 11b), characteristic of photon-assisted small-polaron hopping. At energies near 0.42 eV, absorption bands corresponding to water and/or hydroxyl vibrational modes were observed.[61,62] Additionally, two very reproducible narrow bands at ~0.2 and ~0.3 eV were present and are presumed to be α-Fe_2O_3 overtone or combination

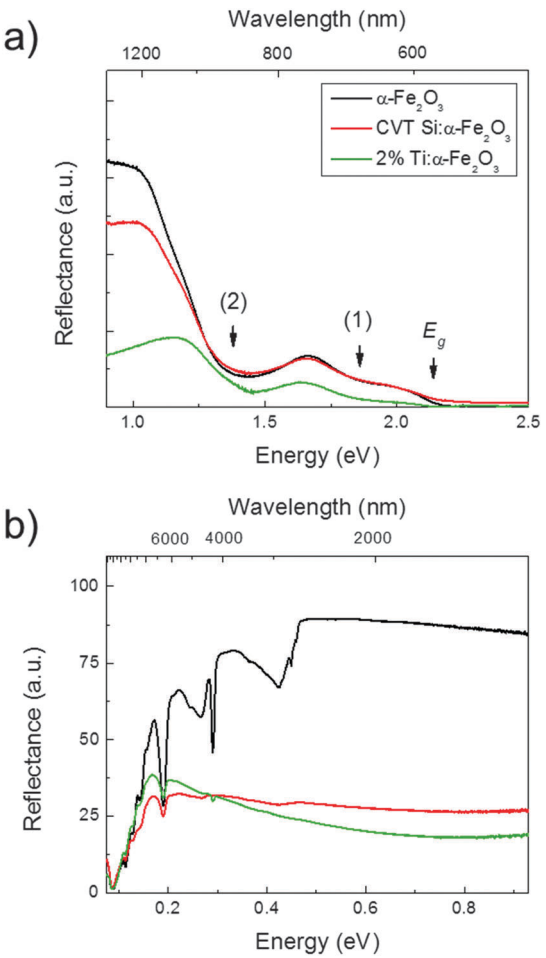

Fig. 11 Reflectance *vs.* photon energy of undoped α-Fe_2O_3, pulverized Si:α-Fe_2O_3 crystals grown by CVT and Ti:α-Fe_2O_3 powder synthesized by a solid-state route in the (a) visible and near-infrared regions and (b) mid-infrared at room temperature. Differences between the magnitude of the reflectance between (a) and (b) in the overlap region, esp. for Si:Fe_2O_3 were possibly due to different mass loadings between the techniques used for the different wavelength ranges.

bands, but their assignment cannot be definitively made at this time. These low energy features are common to all samples, but are most prominent in the undoped powder spectrum; being greatly attenuated and nearly washed out in the spectra of the doped compounds. We ascribe this large drop in reflectance to broad IR absorption bands in Si:α-Fe_2O_3 and Ti:α-Fe_2O_3.

Small-polaron conductors are best thought of as discrete ions with strongly self-trapped carriers. Photon absorption can cause the trapped carrier to be excited from its initial low energy state to a higher energy state on a neighboring ion: a photon-assisted small-polaron hop.[19,63] This broad peak is centered at $\sim 4E_a$,[63] or at energies greater than $\sim$0.5 eV in Si:α-Fe_2O_3 based on our conductivity measurements (see ESI† for detailed calculations). Indeed, broad adsorption was observed across the infrared range in the doped samples and could be acceptably fit by two Gaussian curves centered at $\sim$0.4 eV and $\sim$0.8 eV (see Section S3 and Fig. S5 in the ESI†). As only an estimate of the transfer energy, t, can be made we tentatively assign the peak at 0.8 eV to small-polaron absorption. The width of the small-polaron absorption peak is related to the atoms' thermal displacement, being most narrow at low temperatures and becoming broader as the temperature is increased. Temperature-dependent experiments would be necessary to fully decouple small-polaron absorption from any low energy crystal field or defect-related transitions. However, in the context of our transport analyses we believe its assignment to be reasonable. The reflectance did not scale proportionally between the single crystalline and nominal doping of polycrystalline samples, but as previously mentioned, the effects of M^{4+}-incorporation are often more strongly evident in single crystals compared to polycrystalline samples.[43]

Many properties of our Si:α-Fe_2O_3 samples are comparable to Ti:α-Fe_2O_3 samples in the literature; specifically the conductivity activation energies, behavior of the Seebeck coefficient and optical transitions. However, photoanodes made from these materials vary greatly, with Si proving the superior dopant in some cases[16,17] and Ti in others.[64] Our results imply that differences between these materials' PEC performance must be a result of parameters not considered here, *e.g.* microstructure, carrier recombination or hole transport.

4. Conclusions

In summary, we have synthesized single crystals of Si:Fe_2O_3 *via* chemical vapor transport and showed their electronic and optical properties to be consistent with Si donors creating electron small polarons. Basal plane transport was characterized by conductivity measurements and found to be in good agreement with the adiabatic small polaron-hopping model above the magnetic transition temperature. In the weak ferromagnetic state, the Hall effect was dominated by the weak magnetism of hematite. Below T_M, a larger barrier to hopping was observed, suggesting a more difficult hopping path is now preferred. In this regime, the Hall effect was conventional at low fields, yielding a negative Hall coefficient and Hall mobility that was temperature independent and on the order of 10^{-1} cm^2 V^{-1} s^{-1}. The Seebeck coefficient was negative and its magnitude increased with increasing temperature, suggesting that Si was fully ionized in the temperature range studied. Optical measurements revealed broad infrared absorption, again consistent with electrons forming small polarons. The conductivity, Seebeck, Hall effect and mid-IR absorption experiments presented here represent a thorough and general framework for the analysis of small-polaron transport. Future work should focus on evaluating transport properties over a wider range of doping concentrations and investigating transport anisotropy in doped hematite.

Acknowledgements

The authors gratefully acknowledge the U.S. Department of Energy (DOE) Grant DE-FG02-09ER16119 and Welch Foundation Grant F-1436. We thank A. J. Bard and J. Y. Kim for the use of the three-zone furnace used in this work and D. Emin for useful discussions. A. J. E. R. acknowledges the Hemphill-Gilmore Endowed fellowship for financial support. J.-S. Z. was supported by NSF MIRT DMR 1122603. Finally, we acknowledge B. A. Korgel for help with diffuse reflectance vis-NIR spectroscopy measurements. Work at PNNL was supported in part by the U.S. Department of Energy, National Nuclear Security Administration, Office of Defense Nuclear Nonproliferation R&D (NA-22). PNNL is operated by Battelle for the U.S. DOE under Contract DE-AC05-76RLO1830.

Notes and references

1 R. van de Krol and M. Grätzel, *Photoelectrochemical Hydrogen Production*, 2012.
2 K. Sivula, F. Le Formal and M. Grätzel, *ChemSusChem*, 2011, **4**, 432–449.
3 A. G. Joly, J. R. Williams, S. A. Chambers, G. Xiong, W. P. Hess and D. M. Laman, *J. Appl. Phys.*, 2006, **99**, 053521.
4 A. Bosman and H. Van Daal, *Adv. Phys.*, 1970, **19**, 1–117.
5 N. T. Hahn and C. B. Mullins, *Chem. Mater.*, 2010, **22**, 6474–6482.
6 W. D. Chemelewski, N. T. Hahn and C. B. Mullins, *J. Phys. Chem. C*, 2012, **116**, 5255–5261.
7 Y.-S. Hu, A. Kleiman-Shwarsctein, A. J. Forman, D. Hazen, J.-N. Park and E. W. McFarland, *Chem. Mater.*, 2008, **20**, 3803–3805.
8 Y. Ling, G. Wang, D. A. Wheeler, J. Z. Zhang and Y. Li, *Nano Lett.*, 2011, **11**, 2119–2125.
9 I. Cesar, K. Sivula, A. Kay, R. Zboril and M. Grätzel, *J. Phys. Chem. C*, 2008, **113**, 772–782.
10 G. E. Brown, V. E. Henrich, W. H. Casey, D. L. Clark, C. Eggleston, A. Felmy, D. W. Goodman, M. Grätzel, G. Maciel, M. I. McCarthy, K. H. Nealson, D. A. Sverjensky, M. F. Toney and J. M. Zachara, *Chem. Rev.*, 1998, **99**, 77–174.
11 J. E. Katz, X. Zhang, K. Attenkofer, K. W. Chapman, C. Frandsen, P. Zarzycki, K. M. Rosso, R. W. Falcone, G. A. Waychunas and B. Gilbert, *Science*, 2012, **337**, 1200–1203.
12 B. Zhao, T. C. Kaspar, T. C. Droubay, J. McCloy, M. E. Bowden, V. Shutthanandan, S. M. Heald and S. A. Chambers, *Phys. Rev. B: Condens. Matter Mater. Phys.*, 2011, **84**, 245325.

13 E. Gharibi, A. Hbika, B. Dupre and C. Gleitzer, *Eur. J. Solid State Inorg. Chem.*, 1990, **27**, 647–658.
14 A. J. E. Rettie, W. D. Chemelewski, J. Lindemuth, J. S. McCloy, L. G. Marshall, J. Zhou, D. Emin and C. B. Mullins, *Appl. Phys. Lett.*, 2015, **106**, 022106.
15 A. J. E. Rettie, H. C. Lee, L. G. Marshall, J.-F. Lin, C. Capan, J. Lindemuth, J. S. McCloy, J. Zhou, A. J. Bard and C. B. Mullins, *J. Am. Chem. Soc.*, 2013, **135**, 11389–11396.
16 J. Houlihan, T. Pannaparayil, H. Burdette, D. Madacsi and R. Pollock, *Mater. Res. Bull.*, 1985, **20**, 163–177.
17 J. Kennedy, R. Shinar and J. P. Ziegler, *J. Electrochem. Soc.*, 1980, **127**, 2307–2309.
18 S. D. Tilley, M. Cornuz, K. Sivula and M. Grätzel, *Angew. Chem., Int. Ed.*, 2010, **49**, 6405–6408.
19 D. Emin, *Polarons*, Cambridge University Press, New York, 1st edn, 2013.
20 V. Bogomolov and D. Mirlin, *Phys. Status Solidi B*, 1968, **27**, 443–453.
21 A. Machida, Y. Moritomo and A. Nakamura, *Phys. Rev. B: Condens. Matter Mater. Phys.*, 1998, **58**, R4281.
22 L. Bjaalie, D. Ouellette, P. Moetakef, T. Cain, A. Janotti, B. Himmetoglu, S. Allen, S. Stemmer and C. Van de Walle, *Appl. Phys. Lett.*, 2015, **106**, 232103.
23 A. Dhar and A. Mansingh, *J. Appl. Phys.*, 1990, **68**, 5804–5809.
24 M. Binnewies, R. Glaum, M. Schmidt and P. Schmidt, *Chemical vapor transport reactions*, Walter de Gruyter, 2012.
25 T. J. Johnson, B. E. Bernacki, R. L. Redding, Y.-F. Su, C. S. Brauer, T. L. Myers and E. G. Stephan, *Appl. Spectrosc.*, 2014, **68**, 1224–1234.
26 T. L. Myers, C. S. Brauer, Y.-F. Su, T. A. Blake, R. G. Tonkyn, A. B. Ertel, T. J. Johnson and R. L. Richardson, *Appl. Opt.*, 2015, **54**, 4863–4875.
27 F. J. Morin, *Phys. Rev.*, 1951, **83**, 1005–1010.
28 P. Peshev, A. Toshev, G. Krabbes, U. Gerlach and H. Opperman, *J. Cryst. Growth*, 1984, **66**, 147–155.
29 C. Sanchez, K. Sieber and G. Somorjai, *J. Electroanal. Chem.*, 1988, **252**, 269–290.
30 L. W. Finger and R. M. Hazen, *J. Appl. Phys.*, 1980, **51**, 5362–5367.
31 R. M. Cornell and U. Schwertmann, *The iron oxides: structure, properties, reactions, occurrences and uses*, John Wiley & Sons, 2003.
32 I. R. Beattie and T. R. Gilson, *J. Chem. Soc. A*, 1970, 980–986.
33 S.-H. Shim and T. S. Duffy, *Am. Mineral.*, 2002, **87**, 318–326.
34 D. De Faria, S. Venâncio Silva and M. De Oliveira, *J. Raman Spectrosc.*, 1997, **28**, 873–878.
35 M. Massey, U. Baier, R. Merlin and W. Weber, *Phys. Rev. B: Condens. Matter Mater. Phys.*, 1990, **41**, 7822.
36 D. Benjelloun, J.-P. Bonnet, J.-P. Doumerc, J.-C. Launay, M. Onillon and P. Hagenmuller, *Mater. Chem. Phys.*, 1984, **10**, 503–518.
37 J. Launay and G. Horowitz, *J. Cryst. Growth*, 1982, **57**, 118–124.
38 K. Momma and F. Izumi, *J. Appl. Crystallogr.*, 2011, **44**, 1272–1276.
39 K. Honda and T. Sone, *Sci. Rep. Tohoku Imp. Univ.*, 1914, **3**, 223.
40 J. B. Goodenough, *Prog. Solid State Chem.*, 1971, **5**, 145–399.
41 J. Artman, J. Murphy and S. Foner, *Phys. Rev.*, 1965, **138**, A912.
42 A. H. Morrish, *Canted antiferromagnetism: hematite*, World Scientific, 1994.
43 N. Curry, G. Johnston, P. Besser and A. Morrish, *Philos. Mag.*, 1965, **12**, 221–228.
44 P. Flanders and J. Remeika, *Philos. Mag.*, 1965, **11**, 1271–1288.
45 D. Emin and T. Holstein, *Ann. Phys.*, 1969, **53**, 439–520.
46 K. M. Rosso, D. M. Smith and M. Dupuis, *J. Chem. Phys.*, 2003, **118**, 6455.
47 P. Liao and E. A. Carter, *J. Appl. Phys.*, 2012, **112**, 013701.
48 R. K. Quinn, R. D. Nasby and R. J. Baughman, *Mater. Res. Bull.*, 1976, **11**, 1011–1017.
49 S. A. Baily and D. Emin, *Phys. Rev. B: Condens. Matter Mater. Phys.*, 2006, **73**, 165211.
50 N. L. H. Liu and D. Emin, *Phys. Rev. Lett.*, 1979, **42**, 71.
51 N.-L. H. Liu and D. Emin, *Phys. Rev. B: Condens. Matter Mater. Phys.*, 1984, **30**, 3250.
52 S. V. Ovsyannikov, N. V. Morozova, A. E. Karkin and V. V. Shchennikov, *Phys. Rev. B: Condens. Matter Mater. Phys.*, 2012, **86**, 205131.
53 C. L. Ransom, PhD thesis, Montana State University, 1968.
54 K. Vlasov and E. Rozenberg, *Sov. Phys.-Solid State*, 1980, **22**, 967–969.
55 G. Acket and J. Volger, *Physica*, 1966, **32**, 1543–1550.
56 V. V. Shchennikov, S. V. Ovsyannikov, A. E. Karkin, S. Todo and Y. Uwatoko, *Solid State Commun.*, 2009, **149**, 759–762.
57 R. Voskanyan, R. Levitin and V. Shchurov, *Sov. Phys.-JETP*, 1968, **26**, 302–304.
58 T. Kaneko and S. Abe, *J. Phys. Soc. Jpn.*, 1965, **20**, 2001–2006.
59 L. A. Marusak, R. Messier and W. B. White, *J. Phys. Chem. Solids*, 1980, **41**, 981–984.
60 F. Morin, *Phys. Rev.*, 1954, **93**, 1195.
61 R. N. Clark, G. A. Swayze, R. Wise, K. E. Livo, T. M. Hoefen, R. F. Kokaly and S. J. Sutley, *USGS Digital Spectral Library splib06a*, U.S. Geological Survey, 2007.
62 V. C. Farmer, *Infrared spectra of minerals*, Mineralogical society, 1974.
63 D. Emin, *Phys. Rev. B: Condens. Matter Mater. Phys.*, 1993, **48**, 13691.
64 J. A. Glasscock, P. R. Barnes, I. C. Plumb and N. Savvides, *J. Phys. Chem. C*, 2007, **111**, 16477–16488.